



# Overtuning photoreduction product of CO<sub>2</sub> by defect- and COOH-functionalized multi-wall carbon nanotubes

Peng Liu<sup>a</sup>, Lin Niu<sup>b,c</sup>, Yu-Long Men<sup>a</sup>, Chong Peng<sup>a,\*</sup>, Zheng Liu<sup>b,\*</sup>, Xin-Yu Meng<sup>c</sup>, Yun-Xiang Pan<sup>a,c,\*\*</sup>

<sup>a</sup> School of Electronic Information and Electrical Engineering, Shanghai Jiao Tong University, Shanghai 200240, China

<sup>b</sup> School of Materials Science and Engineering, Nanyang Technological University, Singapore 639798, Singapore

<sup>c</sup> Department of Chemical Engineering, School of Chemistry and Chemical Engineering, Shanghai Jiao Tong University, Shanghai 200240, China

## ARTICLE INFO

### Keywords:

Carbon dioxide  
Photoreduction  
Methanol  
Carbon nanotube  
Functional group

## ABSTRACT

We functionalize MWCNTs with defects and COOH groups to form MWCNTs30 through a novel discharge process. In the photoreduction of CO<sub>2</sub> with pure H<sub>2</sub>O in the absence of sacrificial reagent, with CdS as light absorber, MWCNTs30 triggers a selective CH<sub>3</sub>OH production, with a CH<sub>3</sub>OH selectivity of 100% and an internal quantum efficiency of 3.9%, but CO is the only C-based product by using pristine MWCNTs without functionalization. The defects on MWCNTs30 are active sites for enhancing CO<sub>2</sub> adsorption, H<sub>2</sub>O dissociation to produce H and H transfer to CO<sub>2</sub>, thus boosting CO<sub>2</sub> hydrogenation to CH<sub>3</sub>OH. The COOH groups on MWCNTs30 provide H for promoting CO<sub>2</sub> hydrogenation to CH<sub>3</sub>OH. The multiple roles of defects and COOH groups overturn the photoreduction product from CO to CH<sub>3</sub>OH. The results open a new way to achieve more efficient photoreduction of CO<sub>2</sub> in the absence of noble metal and sacrificial reagent.

## 1. Introduction

Photoreduction of CO<sub>2</sub> can not only alleviate CO<sub>2</sub> emission but also produce valuable chemicals, e.g. CH<sub>3</sub>OH [1]. Yet, to date, its efficiency still remains far below the commercialization need. A problem is that the photoreduction product is usually a complex mixture including many species [1–3]. This reduces the selectivity and yield of target product. Another problem of the photoreduction is that sacrificial reagent, e.g. triethanolamine, is generally used to separate the photogenerated electron-hole pairs [1–3]. But sacrificial reagent complicates the reaction system, thus making the purification and application of photoreduction product difficult. Photocatalysts boosting selective photoreduction of CO<sub>2</sub> without sacrificial reagent are thereby highly desired.

Many photocatalysts have been developed for photoreduction of CO<sub>2</sub> in the absence of sacrificial reagents [4–8]. Through growing leaf-like zeolitic imidazolate frameworks (ZIF-L) on dendritic-like TiO<sub>2</sub>/C nanofibers, Zhou et al. prepared a TiO<sub>2</sub>/C@ZnCo-ZIF-L photocatalyst for photoreduction of CO<sub>2</sub> [4]. In the absence of sacrificial reagents, TiO<sub>2</sub>/C@ZnCo-ZIF-L resulted in a CO production rate of 28.6 μmol h<sup>-1</sup>

g<sup>-1</sup> and a CO selectivity of 99% [4]. Huang et al. found that a laminar core-shell PCN-222-Ni@UiO-67-NH<sub>2</sub> photocatalyst led to a photoreduction of CO<sub>2</sub> to formic acid (HCOOH) in the absence of sacrificial reagents, with a HCOOH production rate of 146.0 μmol h<sup>-1</sup> g<sup>-1</sup> [5]. By using a well-defined porous hyper-crosslinked polymer-TiO<sub>2</sub>-graphene composite photocatalyst, Wang et al. achieved a photoreduction of CO<sub>2</sub> to CH<sub>4</sub> in the absence of sacrificial reagents, with a CH<sub>4</sub> evolution rate of 27.62 μmol h<sup>-1</sup> g<sup>-1</sup> [6]. In spite of the wide studies, the photoreduction efficiency of CO<sub>2</sub> in the absence of sacrificial reagents is still low, and requires further improvement. In addition, the photoreduction mechanism of CO<sub>2</sub> in the absence of sacrificial reagents is unclear, and needs more detailed understandings.

Multi-wall carbon nanotubes (MWCNTs) have attracted great attentions in photocatalysis [9–13]. MWCNTs are highly conductive, and superior in capturing electrons (one electron for every 32 C), thus facilitating the separation of photogenerated electron-hole pairs [9]. Besides, MWCNTs are flexible in activating CO<sub>2</sub> and H<sub>2</sub>O which are common reactants in photocatalysis [9–13]. These make MWCNTs efficient in boosting photocatalytic reactions [9–13]. For example, by using a g-C<sub>3</sub>N<sub>4</sub> photocatalyst supported on a composite containing

\* Corresponding authors.

\*\* Corresponding author at: School of Electronic Information and Electrical Engineering, Shanghai Jiao Tong University, Shanghai 200240, China.

E-mail addresses: [pengchong@dlut.edu.cn](mailto:pengchong@dlut.edu.cn) (C. Peng), [z.liu@ntu.edu.sg](mailto:z.liu@ntu.edu.sg) (Z. Liu), [yxpan81@sjtu.edu.cn](mailto:yxpan81@sjtu.edu.cn) (Y.-X. Pan).

mesoporous carbon and MWCNTs, Wang et al. observed an efficient photoreduction of  $\text{CO}_2$  to CO and  $\text{CH}_4$  [11]. Another example, Shu et al. found that the CO and  $\text{CH}_4$  yields in the photoreduction of  $\text{CO}_2$  on a  $\text{CsPbBr}_3/\text{MWCNTs}$  photocatalyst were 3.14 and 2.13 times higher than those on pristine  $\text{CsPbBr}_3$  without MWCNTs, respectively [12]. MWCNTs played as electron acceptors to inhibit the recombination of the charge carriers photogenerated on  $\text{CsPbBr}_3$ , thus improving the photocatalytic performance of  $\text{CsPbBr}_3/\text{MWCNTs}$  [12]. In these studies, MWCNTs were applied as supports of photocatalysts or/and as bridges for transferring photogenerated charge carriers between light absorbers and species providing catalytic active centers. Besides, sacrificial reagents were used in these studies. Application of MWCNTs in the photoreduction of  $\text{CO}_2$  in the absence of sacrificial agents, with MWCNTs providing catalytic active sites, has not been reported yet.

Herein, we functionalize MWCNTs by defect and COOH via a novel discharge process (Figs. S1 and S2). Traditional methods for functionalizing MWCNTs by defects and COOH often used heating or/and harmful reagents, e.g.  $\text{HNO}_3$  and  $\text{H}_2\text{SO}_4$  [14,15]. The discharge process is completely different from traditional methods. The discharge process is conducted in the presence of  $\text{O}_2$  and  $\text{H}_2\text{O}$ , without heating and without any harmful reagent. The discharge process produces abundant electrons with energy of 5–10 eV [16–19]. Collision of the discharge-produced electrons with  $\text{O}_2$ ,  $\text{H}_2\text{O}$  and MWCNTs leads to reactions among the species, thus creating defect and COOH on MWCNTs [17–19]. As compared with traditional methods, the discharge process is green and easy to control. Moreover, the functional group features on MWCNT can be tuned by simply changing the operation conditions of the discharge process. The MWCNTs functionalized via the discharge process show significantly improved performance in the photoreduction of  $\text{CO}_2$  with pure  $\text{H}_2\text{O}$  in the absence of sacrificial reagents, with CdS as light absorbers. The defects on MWCNTs provide active sites for  $\text{CO}_2$  adsorption and conversion, and the synergistic effect between defects and COOH groups on MWCNTs overturns the photoreduction product from CO to  $\text{CH}_3\text{OH}$ .

## 2. Experimental and calculations

### 2.1. Catalyst preparations

Pristine MWCNTs (MWCNTs0) with diameters of 30–50 nm were purchased from Chengdu Organic Chemistry Co., LTD, China, and were further functionalized by the discharge process. Fig. S1 schematically shows the set-up for the discharge-driven functionalization process, and an image taking during the discharge process is given in Fig. S2. The discharge-driven functionalization process was carried out as follows. Firstly, 500 mg MWCNTs were dispersed in 2 mL deionized (DI) water under ultrasonication for 30 min to form a mixture. Secondly, the mixture was put into the discharge chamber (Fig. S1). Thirdly, a power of 200 W was applied on the electrodes of the discharge chamber to trigger the discharge process. Fourthly, the discharge-driven functionalization process was carried out for 10 cycles, with each cycle proceeding for 3 min and total time of the discharge-driven functionalization equaling to 30 min, by using  $\text{O}_2$  as working gas, leading to MWCNTs30. To ensure that the sample was functionalized uniformly, after each cycle, the sample was taken out from the discharge chamber, and stirred for 2 min. For comparison, we also prepared MWCNTs5, MWCNTs15 and MWCNTs45 through functionalizing MWCNTs by conducting the discharge-driven functionalization for 5, 15 and 45 min, respectively.

The reagents used for fabricating CdS nanoparticles, including CdO, oleic acid (OA), octadecene (ODE) and trioctylphosphine (TOP) in analytical grade purity, were purchased from Alfa Aesar and used as received without further treatment. The CdS nanoparticles were fabricated through the following procedures. Firstly, CdO (0.512 g), OA (5.0 mL) and ODE (15.0 mL) were mixed in a 3-neck flask (50 mL) and heated under an argon atmosphere. When the temperature of the mixture

reaches to 300 °C, the TOP solution of sulfur (2 M, 1 mL) was quickly injected into the mixture, and the temperature was kept at 260 °C for 5 min, followed by cooling to room temperature naturally. Then, the sample was washed with methanol and DI water for several times, and dried under vacuum at 25 °C for 12 h, producing the CdS nanoparticles.

To fabricate the CdS/MWCNTs30 photocatalyst, MWCNTs30 (10 mg) and CdS nanoparticles (40 mg) were firstly dispersed in an aqueous solution under ultrasonication for 1 h. Then, the mixture was centrifuged to collect the solid. Next, the solid was washed with ethanol and DI water for several times and then dried under vacuum at 25 °C for 12 h, leading to CdS/MWCNTs30. By using the procedures similar to those for CdS/MWCNTs30, CdS nanoparticles were also loaded on MWCNTs0, MWCNTs5, MWCNTs15 and MWCNTs45 to form CdS/MWCNTs0, CdS/MWCNTs5, CdS/MWCNTs15 and CdS/MWCNTs45, respectively. In addition, for clarity, the photocatalysts after reactions were named as A-CdS/MWCNTs0, A-CdS/MWCNTs5, A-CdS/MWCNTs15, A-CdS/MWCNTs30 and A-CdS/MWCNTs45, respectively.

### 2.2. Catalyst characterizations

Transmission electron microscopy (TEM) images were obtained on a JEOL2100F field emission microscope operating at 200 kV. High-resolution TEM (HRTEM), high-angle annular dark field (HAADF) and elemental mapping images were acquired on a JEOL ARM200F (JEOL, Tokyo, Japan). X-ray diffraction (XRD) patterns were observed on a Bruker D8 ADVANCE Da Vinci (Cu K $\alpha$ ). Surface areas of materials were explored on an ASAP 2020 analyzer (Micromeritics, Norcross, USA) and calculated by using the Brunauer-Emmett-Teller (BET) method. X-ray photoelectron spectroscopy (XPS) observations were conducted on an ESCA 2000 X-ray photoelectron spectrophotometer (VG Scientific, monochromated Mg KR radiation). XPS peaks were calibrated by C 1 s peak at 284.6 eV. Raman spectra were obtained at room temperature on a Renishaw inVia Qontor Raman spectrometer with a laser for excitation ( $\lambda = 785$  nm) and a laser power of 250 mW. Electron paramagnetic resonance (EPR) spectra were recorded on a Bruker A300 electron paramagnetic spectrometer operating at 9.820 GHz. Electrochemical measurements were done on an electrochemical workstation (CHI760E, CH Instrument, Inc.) at room temperature. Fourier transform infrared (FTIR) observations were done on a Spectrum 3 FTIR spectrometer (PerkinElmer) with a diffuse reflectance accessory and a Mercury-Cadmium-Tellurium (MCT) detector cooling by liquid nitrogen. The *in-situ* FTIR spectra were recorded through the following steps. Firstly, 50 mg photocatalyst was put in the FTIR cell, and purged with Ar at 200 °C for 2 h to remove water and impurities. Secondly, the FTIR cell temperature was lowered to room temperature in Ar, and then background spectra were recorded. Thirdly, a  $\text{CO}_2/\text{Ar}$  mixture with 10 vol%  $\text{CO}_2$  was injected into the FTIR cell. All FTIR spectra were recorded at room temperature with a spectral resolution of 4  $\text{cm}^{-1}$  and 64 scans. UV-3101 Shimadzu spectrophotometer was applied to observe the UV–visible diffuse reflectance spectra of the photocatalysts. Temperature-programmed desorption (TPD) spectra were obtained in a quartz-tube fixed-bed reactor (inner diameter: 4 mm) placed inside an electrical furnace under atmosphere of Ar. The flow rate of the carrier gas (Ar) and heating rate of the furnace were set at 80  $\text{mL s}^{-1}$  and 5  $\text{K min}^{-1}$ , respectively. The amounts of CO and CO desorbed from the carbon nanotubes were analyzed by a gas chromatography (Agilent 7890 A) with thermal conductivity (TCD) detectors.

An ASAP 2020 analyzer (Micromeritics, Norcross, GA, USA) was used to study the  $\text{CO}_2$  adsorption capacity of the samples. The pressure ranged from 0 to 1.01 bar. The adsorption experiments proceeded at 25 °C by using circulated water. Prior to the adsorption experiments, the samples were degassed at 200 °C for 12 h. Nuclear magnetic resonance (NMR) spectra were acquired on a 600 MHz Bruker NMR spectrometer. All the chemical shifts were referenced to tetramethyl silane, and all NMR spectra were treated by using the Topspin software. The ultraviolet photoelectron spectroscopy (UPS) results were obtained on an X-ray

Photoelectron Spectroscopy meter (Al K $\alpha$ , Kratos AXIS Ultra DLD) with a base pressure of  $5.0 \times 10^{-9}$  Torr and an X-ray tube power of 130 W. Electrochemical studies, including photocurrent and Mott-Schottky plots, were measured on a CHI660A electrochemical workstation in a Na<sub>2</sub>SO<sub>4</sub> solution (0.1 M) using a 300 W Xe-lamp with a cut-off filter ( $\lambda \geq 420$  nm), with a constant potential of 0.35 V vs. standard electrode (SCE). The solution and light source used for measuring photocurrents are similar to those for the photocatalytic reactions. The electrochemical workstation includes three electrodes. A Pt plate and a saturated calomel electrode were used as the counter electrode and reference electrode, respectively. For preparing the working electrode, with a surface area of

1.44 cm<sup>2</sup> exposed to electrolyte, 1 mg sample was first dispersed in 1 mL ethanol containing naphthol (0.05 wt%) under ultrasonication. Then, the suspension was dropped onto indium tin oxide glasses and dried at room temperature.

### 2.3. Photocatalytic reaction

Photoreduction of CO<sub>2</sub> with H<sub>2</sub>O was performed in a closed gas circulation-evacuation reactor. The set-up used for conducting the photoreduction was illustrated in Fig. S3. Before reaction, the following steps were carried out. Firstly, 100 mg photocatalyst was dispersed in

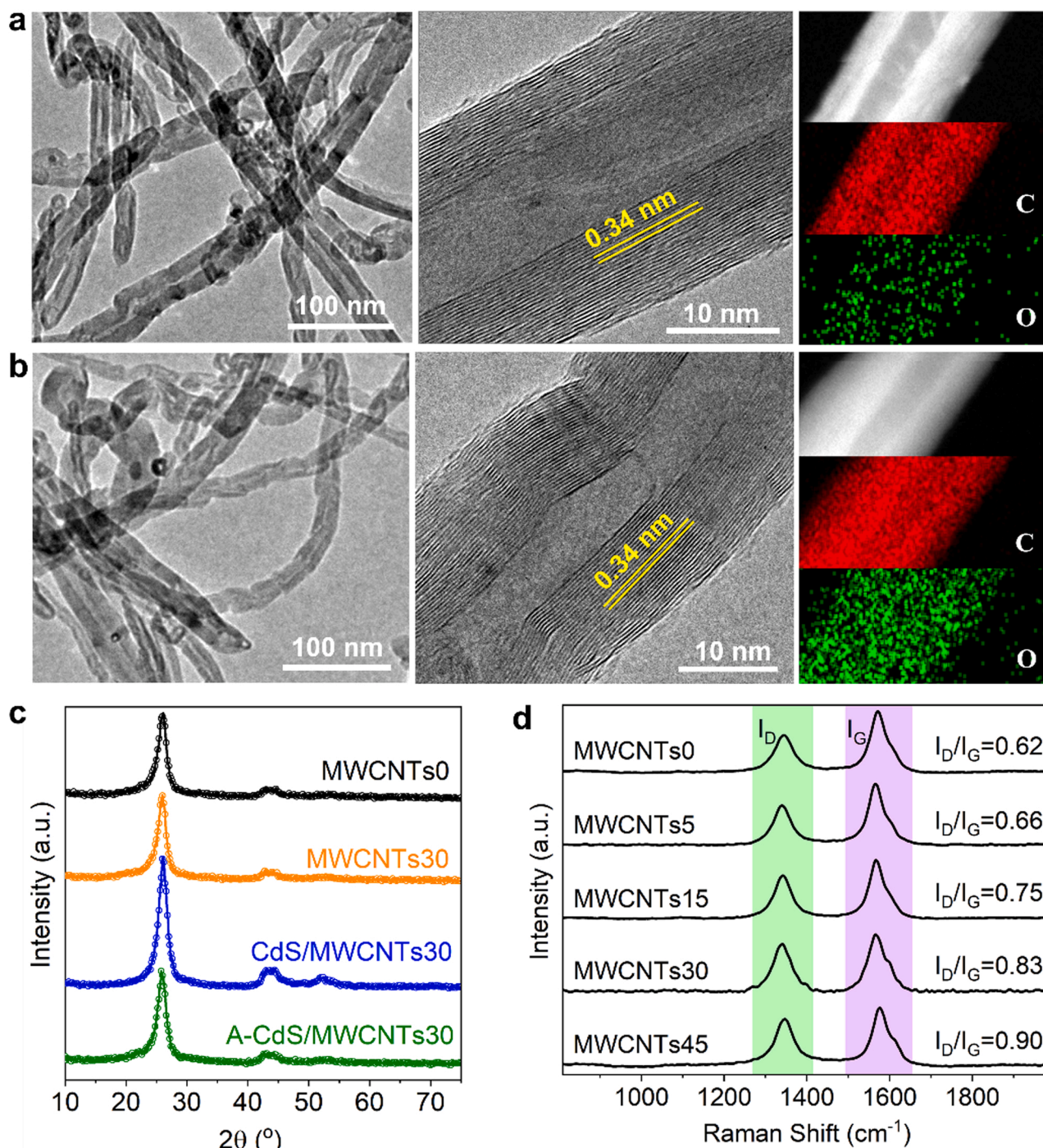


**Fig. 1.** (a) TEM, HRTEM and elemental mapping images of MWCNTs0. (b) TEM, HRTEM and elemental mapping images of MWCNTs30. (c) XRD patterns. (d) Raman spectra.



water (100 mL). Secondly, the reactor was evacuated and refilled with pure CO<sub>2</sub> for three times to remove the air inside. Finally, the reactor was filled with CO<sub>2</sub> until the pressure reached to 1.01 bar. During the photoreduction, the reactor was irradiated under a Xe-lamp (300 W, light intensity: 100 mW cm<sup>-2</sup>) with a cut-off filter ( $\lambda \geq 420$  nm) under vigorous stirring, and the temperature of the reactor was kept at 25 °C by using cooling water. The photoreduction products were analyzed by gas chromatography (Agilent 7890 A) with both flame ionization (FID) and thermal conductivity (TCD) detectors. The FID detector and an Agilent HPPLLOT Q capillary column were used for analyzing methanol, while the TCD detector and a Porapak Q packed column was used for analyzing H<sub>2</sub>, O<sub>2</sub>, CO<sub>2</sub>, CO and CH<sub>4</sub>. Ar was used as the carrier gas. The GC was switched between the two columns by using a four-port valve. To determine the source of the carbon in products, isotopic experiments were carried out under identical reaction conditions, and products were analyzed by gas chromatography-mass spectrometry (GC-MS).

## 2.4. Computational methods

Methods for density functional theory (DFT) calculations were described in the [Supplementary Data](#).

## 3. Results and discussion

### 3.1. Catalyst characterizations

For clarity, the pristine MWCNTs without functionalization are denoted as MWCNTs0 where 0 represents the discharge time. Functionalizing MWCNTs0 by 30 min discharge fabricates MWCNTs30. For comparison, we also prepare MWCNTs5, MWCNTs15 and MWCNTs45 by using 5, 15 and 45 min discharge, respectively. The morphology (TEM images) and XRD pattern of MWCNTs30 are almost the same as those of MWCNTs0 (Fig. 1). Therefore, the discharge-driven functionalization does not change the morphology and crystal structure of MWCNTs. The surface area (110.3 m<sup>2</sup> g<sup>-1</sup>), pore size (19.68 nm) and pore volume (0.55 cm<sup>3</sup> g<sup>-1</sup>) of MWCNTs30 are slightly larger than those of MWCNTs0 (106.8 m<sup>2</sup> g<sup>-1</sup>, 19.52 nm, 0.53 cm<sup>3</sup> g<sup>-1</sup>) (Fig. S4). During the discharge-driven functionalization, collision of the discharge-produced electrons with MWCNTs could create defects and pores on MWCNTs. This could be the origin for the slightly larger surface area, pore size and pore volume of MWCNTs30. The operation condition of the discharge-driven functionalization is mild, with temperature lower than 150 °C and without using strong oxidants like HNO<sub>3</sub> and H<sub>2</sub>SO<sub>4</sub> [16–19]. This helps to maintain the morphology and structure of MWCNTs well during the discharge-driven functionalization, as confirmed by XRD and TEM (Fig. 1). Collision of the discharge-produced electrons with MWCNTs could create pores on MWCNTs, but amount of the created pores could be small, due to the mild operation conditions of the discharge. Thus, the discharge-driven functionalization increases the pore size, pore volume and surface area of MWCNTs, but the increase extents are very small.

The lattice fringe (0.34 nm) observed in HRTEM images of MWCNTs0 and MWCNTs30 is due to the MWCNTs (002) plane (Fig. 1) [9–12]. As implied by elemental mapping images (Fig. 1), MWCNTs30 could have more O-containing groups than MWCNTs0. The Raman spectra of MWCNTs0 and MWCNTs30 show a G band at 1570 cm<sup>-1</sup> and a D band at 1340 cm<sup>-1</sup>, which are due to *sp*<sup>2</sup> C in C=C bond and carbon defect, respectively (Fig. 1d) [20,21]. The intensity ratio of D band to G band, i.e. I<sub>D</sub>/I<sub>G</sub>, on MWCNTs30 (0.83) is higher than that on MWCNTs0 (0.62), indicating that MWCNTs30 has more defects than MWCNTs0 [20,21]. Besides, the I<sub>D</sub>/I<sub>G</sub> ratios of the materials functionalized by different discharge times are in an order of MWCNTs0 < MWCNTs5 < MWCNTs15 < MWCNTs30 < MWCNTs45 (Fig. 1d), showing the formation of more defects at longer discharge processes. The defect content increase at longer discharge processes is further confirmed by EPR spectra where the peak due to carbon defects

becomes stronger with elongating discharge time (Fig. S5) [22].

XPS studies confirm the presence of C and O on MWCNTs0 and MWCNTs30 (Fig. 2a, S6, S7 and S8). The C 1 s XPS spectra of MWCNTs0 and MWCNTs30 can be fitted into peaks at 283.8, 284.5, 285.3, 286.5, 287.9, 288.9 and 290.8 eV, which are due to carbon defect, C=C, C-C, C bonding to OH, carbonyl (C=O), O-C=O in carboxyl (COOH) and  $\pi$ - $\pi^*$  shake-up, respectively (Fig. 2a) [23–26]. Based on C 1 s XPS spectra, the defect and functional group contents are calculated (Table S1). The defect and COOH contents on MWCNTs30 (9.1%, 7.4%) are 2.2- and 3.2-fold higher than those on MWCNTs0 (4.2%, 2.3%), respectively. As compared with MWCNTs0 (5.9%, 4.5%), the contents of OH (6.3%) and C=O (5.2%) on MWCNTs30 increase, but the increase extents are slight. The higher content of O-containing group on MWCNTs30 than that on MWCNTs0 is also revealed by O 1 s XPS spectra (Fig. S8) [27]. Besides, the C 1 s and O 1 s XPS spectra (Figs. S7 and S8) show that the defect and O-containing group contents on the materials get higher at longer discharge-driven functionalization (Table S1). Different from defect and O-containing group, MWCNTs30 has less C=C (54.6%) and C-C (17.4%) than MWCNTs0 (63.7%, 19.4%) (Table S1).

Fig. 2b shows the CO<sub>2</sub> and CO evolution curves recorded in TPD experiments for MWCNTs0 and MWCNTs30. TPD experiment is a qualitative method for analyzing the functional groups on solid materials [28]. Intensity and area of the TPD peak only approximately reflect which functional group could be more, and cannot determine the amount of the functional group exactly [28]. Deconvolution of CO<sub>2</sub> and CO TPD signals for MWCNTs0 and MWCNTs30 are illustrated in Figs. S9 and S10, and areas of the TPD peaks obtained from deconvolution are listed in Table S2. The CO<sub>2</sub> TPD peak at 100–400 °C are caused by COOH, while the CO TPD peaks at 400–700 and 700–900 °C are due to OH and C=O, respectively (Fig. 2b) [28]. Intensity and area of the CO<sub>2</sub> TPD peak for MWCNTs30 (1.0  $\mu\text{mol g}^{-1} \text{s}^{-1}$ , 144.6) are about 10.0 and 11.3 times higher than those for MWCNTs0 (0.1  $\mu\text{mol g}^{-1} \text{s}^{-1}$ , 12.8), indicating that MWCNTs30 has more COOH than MWCNTs0. Intensities and areas of the CO TPD peaks at 400–700 °C (0.09  $\mu\text{mol g}^{-1} \text{s}^{-1}$ , 10.0) and 700–900 °C (0.10  $\mu\text{mol g}^{-1} \text{s}^{-1}$ , 8.0) for MWCNTs30 are close to those at 400–700 °C (0.08  $\mu\text{mol g}^{-1} \text{s}^{-1}$ , 10.0) and 700–900 °C (0.08  $\mu\text{mol g}^{-1} \text{s}^{-1}$ , 8.0) for MWCNTs0, respectively. Therefore, the OH and C=O contents on MWCNTs30 could be similar to those on MWCNTs0. For MWCNTs30, CO<sub>2</sub> TPD peak is much stronger than CO TPD peaks, implying the much higher content of COOH than those of OH and C=O (Fig. 2b). An O-containing group content increase at longer discharge-driven functionalization is evidenced by the enhanced CO<sub>2</sub> and CO TPD peaks (Figs. S9 and S10, Table S2). Peaks at 3340, 1722, 1590, 1391 and 1128 cm<sup>-1</sup> on the FTIR spectra are assigned to the adsorbed H<sub>2</sub>O, O-C=O in COOH, C=C close to COOH, O-H in C-OH and C-O in C-OH, respectively (Fig. 2c) [29–32]. MWCNTs30 shows stronger FTIR peaks of COOH than MWCNTs0, but similar FTIR peaks of OH to MWCNTs0. Hence, MWCNTs30 could have more COOH than MWCNTs0, while OH content on MWCNTs30 could be close to that on MWCNTs0. Besides, FTIR spectra reveal that a longer discharge-driven functionalization produces more COOH on the materials (Fig. 2c). The FTIR and TPD results agree well with the XPS results.

During the discharge-driven functionalization process with H<sub>2</sub>O and O<sub>2</sub>, collision of the discharge-produced electrons with O<sub>2</sub>, H<sub>2</sub>O and MWCNTs leads to reactions among the species, thus creating COOH on MWCNTs [17–19]. The C atom of COOH should be from MWCNTs, and formation of COOH accompanies the dissociation of C-C and C=C bonds in MWCNTs skeleton. This decreases the C-C and C=C contents on MWCNTs, and forms defects on MWCNTs, with some defects close to COOH. Apart from COOH, OH and C=O could also be created on MWCNTs during the discharge process. However, as reflected by XPS, TPD and FTIR spectra, the COOH content on MWCNTs30 could be much higher than that on MWCNTs0, while the OH and C=O contents on MWCNTs30 could be close to those on MWCNTs0. Moreover, on MWCNTs30, the COOH content is higher than the O-H and C=O contents. So COOH could be dominantly formed in the discharge process.

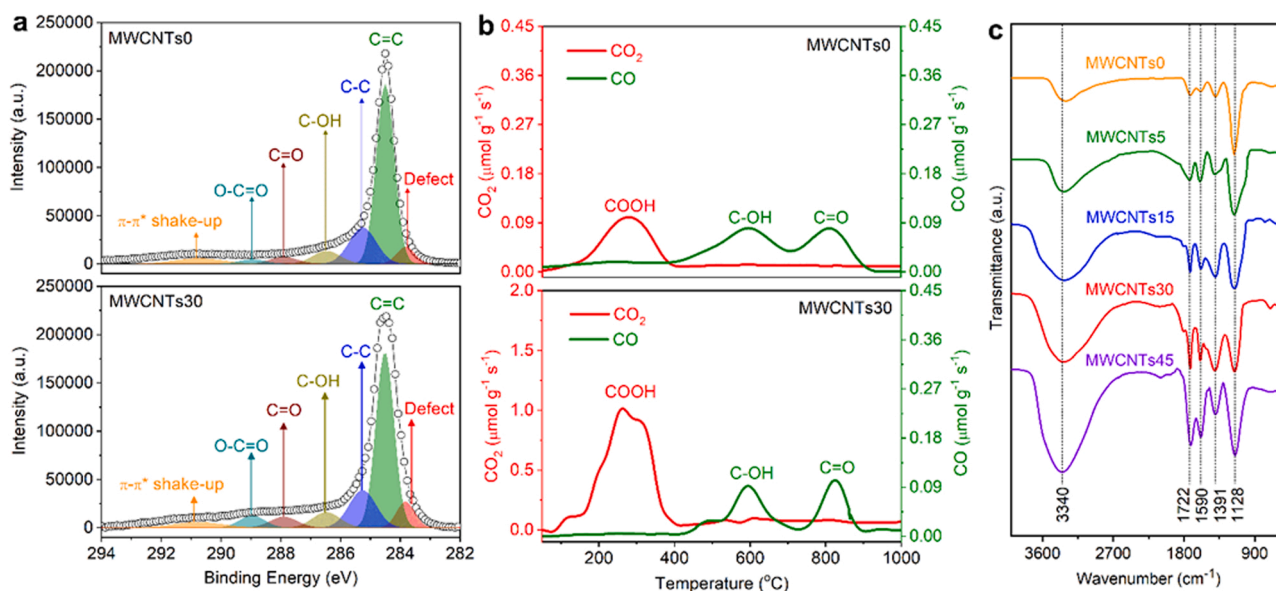


**Fig. 2.** (a) C 1s XPS and (b) TPD spectra of MWCNTs0 and MWCNTs30. (c) FTIR spectra of MWCNTs0, MWCNTs5, MWCNTs15, MWCNTs30 and MWCNTs45.

Besides  $O_2$ ,  $H_2O$  and MWCNTs, no harmful species are used in the discharge process. Moreover, the surface properties MWCNTs can be efficiently tuned by simply changing discharge time (Table S1). So the discharge process is an excellent strategy to tune surface properties of MWCNTs.

CdS nanoparticles are next prepared, and are used as light absorber to decorate MWCNTs0 and MWCNTs30 to fabricate CdS/MWCNTs0 and CdS/MWCNTs30 photocatalysts, respectively. The CdS nanoparticles have an average size of about 5 nm (Fig. S11). On the XRD pattern of CdS nanoparticles, three peaks appear at 26.5, 44.0 and 52.1°, and correspond to the (111), (220) and (311) planes of cubic CdS (JCPDS No. 80-0019) (Fig. S12) [33,34]. Peaks at 26.2, 42.2 and 44.4°, attributed to the (002), (100) and (101) planes of MWCNTs, respectively (JCPDS No. 41-1487) [32], appear on the XRD pattern of CdS/MWCNTs30 (Fig. 1c). It should be noted that the XRD peak at 44.4° on CdS/MWCNTs30 is stronger than that on MWCNTs30 without CdS nanoparticles. This may be caused by the overlap between the XRD peak at 44.4° due to the (101) plane of MWCNTs and the XRD peak at 44.0° due to the (220) plane of CdS. In addition to the peaks of MWCNTs, the XRD pattern of CdS/MWCNTs30 also exhibits a peak at 52.1° characteristic of the (311) plane of cubic CdS [33,34], confirming the presence of CdS nanoparticles on CdS/MWCNTs30. TEM observations further confirm the presence of CdS nanoparticles on CdS/MWCNTs0 and CdS/MWCNTs30 (Fig. 3 and S13). Lattice fringes with distances of 0.34 and 0.35 nm present in the HRTEM image are due to the (002) plane of MWCNTs and the (111) plane of CdS, respectively (Fig. 3b) [18,34,35]. The XPS spectra confirm the presence of C, O, Cd and S on CdS/MWCNTs0 and CdS/MWCNTs30 (Fig. 3d, S14 and S15). The C 1s and O 1s XPS spectra of CdS/MWCNTs0 and CdS/MWCNTs30 are similar to those of MWCNTs0 and MWCNTs30, respectively (Fig. 3d and S15). According to C 1s XPS spectra (Fig. 3d), the defect, C=C, C-C, OH, C=O and COOH contents on CdS/MWCNTs0 and CdS/MWCNTs30 are found to be close to those on MWCNTs0 and MWCNTs30, respectively (Table S1). Therefore, influences of CdS nanoparticles on the surface properties of MWCNTs0 and MWCNTs30 are slight.

### 3.2. Catalytic performance

Photoreduction of  $CO_2$  with pure  $H_2O$  is done in the absence of sacrificial reagent at 25 °C under irradiation of visible light ( $\lambda \geq 420$  nm). Pure CdS, MWCNTs0 and MWCNTs30 have no activity towards the photoreduction. CdS/MWCNTs0 and CdS/MWCNTs30

trigger the photoreduction efficiently (Fig. 4a and 4b). During the photoreduction, CO and  $CH_3OH$  are the C-based products, and other C-based products in both gas and liquid phases, e.g.  $CH_4$  and  $HCOOH$ , are not observed.  $CH_3OH$  and CO selectivity are calculated by the ratio of  $CH_3OH$  and CO in all C-based products, respectively. With increasing CdS mass in photocatalyst, the photocatalytic activity gets higher firstly and then decreases, with the highest activity present on the photocatalyst containing 40 mg CdS (Fig. 4a). On photocatalysts fabricated by loading CdS on MWCNTs functionalized with different discharge times, the CO formation rate is in an order: CdS/MWCNTs0 > CdS/MWCNTs5 > CdS/MWCNTs15 > CdS/MWCNTs30 = CdS/MWCNTs45, but the  $CH_3OH$  formation rate is in an order: CdS/MWCNTs0 < CdS/MWCNTs5 < CdS/MWCNTs15 < CdS/MWCNTs45 < CdS/MWCNTs30 (Fig. 4b). CdS/MWCNTs0 has the highest activity in producing CO ( $4.9 \mu mol h^{-1}$ ), with a CO selectivity of 100 %. NMR study shows that there is no liquid C-based product formed on CdS/MWCNTs0 (Fig. S16). CdS/MWCNTs30 is the most active in  $CH_3OH$  production ( $10.5 \mu mol h^{-1}$ ), with a  $CH_3OH$  selectivity of 100 %. NMR study confirms that, except  $CH_3OH$ , no other liquid C-based product is formed on CdS/MWCNTs30 (Fig. S16). By using the procedure described in Supplementary Data, the internal quantum efficiency (IQE) of CdS/MWCNTs30 in harvesting photons for the redox reactions are calculated to be 3.9%, which is about 6.5-fold higher than that of CdS/MWCNTs0 (0.6%) (Fig. S17). Besides, efficiency of CdS/MWCNTs30 in producing  $CH_3OH$  in photoreduction of  $CO_2$  with pure  $H_2O$  in the absence of sacrificial reagent is better than the photocatalysts widely reported in literature (Table S3).

Photocatalytic stability of CdS/MWCNTs30 is explored by four consecutive cycles with each cycle of 6 h (Fig. 4c). After each cycle, the light irradiation is stopped, the reactor is evacuated and then refilled with  $CO_2$  to 1.01 bar, but no fresh photocatalyst or fresh aqueous solution are introduced and no photocatalyst washing is performed. During the stability experiment, the  $CH_3OH$  selectivity on CdS/MWCNTs30 remains 100%, and no CO is observed on CdS/MWCNTs30 (Fig. 4c). After four cycles, the  $CH_3OH$  yields decreases by 27.8%, from 58.3 to 42.1  $\mu mol$  (Fig. 4c). This may be caused by the amount decrease of catalytic active sites on CdS/MWCNTs30 during the stability experiment. CdS/MWCNTs30 after stability experiment, denoted by A-CdS/MWCNTs30, has a XRD pattern similar to that of fresh CdS/MWCNTs30 (Fig. 1c), indicating that the crystal structure of the photocatalyst does not change during the stability experiment. According to C 1s XPS spectra (Fig. 3d), A-CdS/MWCNTs30 has less defect and COOH, but more C=C, C-C and OH, than fresh CdS/MWCNTs30 (Table S1). The

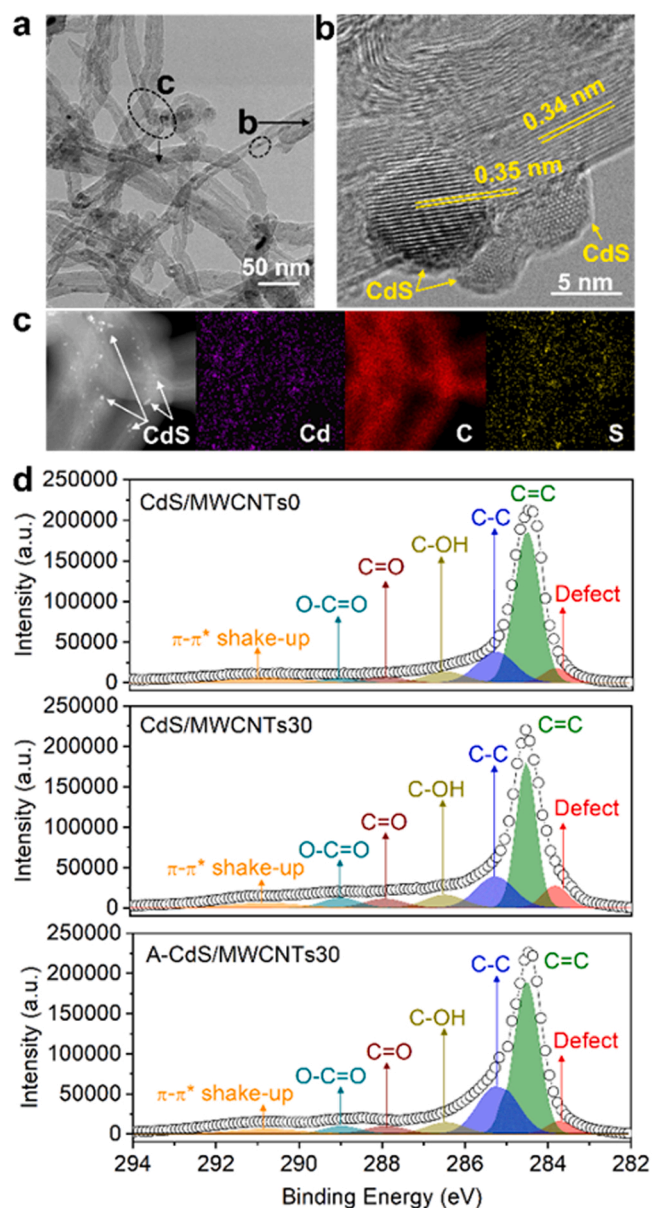


Fig. 3. (a) TEM, (b) HRTEM and (c) elemental mapping images of CdS/MWCNTs30. (d) C 1s XPS spectra of CdS/MWCNTs0, CdS/MWCNTs30 and A-CdS/MWCNTs30.

C=O content on A-CdS/MWCNTs30 is close to that on fresh CdS/MWCNTs30 (Table S1). Thus, during the reaction, some defect and COOH are consumed, while some C=C, C-C and OH are created. In addition, the Cd 3d and S 2p XPS spectra are almost unchanged after stability experiment (Fig. S18), indicating that supporting CdS nanoparticles on MWCNTs30 can efficiently suppress the photocorrosion, decomposition and oxidation of CdS during the photoreduction.

To confirm the origin of CH<sub>3</sub>OH formed on CdS/MWCNTs30, three control experiments are conducted: (i) experiment with CdS/MWCNTs30, CO<sub>2</sub> and H<sub>2</sub>O, but without light; (ii) experiment with CO<sub>2</sub>, H<sub>2</sub>O and light, but without CdS/MWCNTs30; (iii) experiment with CdS/MWCNTs30, H<sub>2</sub>O and light, but without CO<sub>2</sub>. CH<sub>3</sub>OH is not seen in all control experiments, implying that CH<sub>3</sub>OH comes from the photoreduction of CO<sub>2</sub> with H<sub>2</sub>O on CdS/MWCNTs30. Six isotopic experiments (Exps. I, II, III, IV, V and VI) are also done to explore the origin of CH<sub>3</sub>OH. In Exps. I, II and III, MWCNTs30 is prepared by doing the discharge process with O<sub>2</sub> and H<sub>2</sub>O, and defect and COOH are created on MWCNTs30. In Exp. I with <sup>12</sup>CO<sub>2</sub> and H<sub>2</sub>O as photoreduction reactants,

*m/z* signals of H, H<sub>2</sub>, CH, CH<sub>2</sub>, CH<sub>3</sub>, O, OH, H<sub>2</sub>O, CO, CHO, CH<sub>2</sub>O, CH<sub>3</sub>O, CH<sub>3</sub>OH/O<sub>2</sub> and CO<sub>2</sub> appear, indicating that CH<sub>3</sub>OH comes from the photoreduction of CO<sub>2</sub> with H<sub>2</sub>O (Fig. 4d). In Exp. II with <sup>13</sup>CO<sub>2</sub> and H<sub>2</sub>O as photoreduction reactants, *m/z* signals of H, H<sub>2</sub>, <sup>13</sup>CH, <sup>13</sup>CH<sub>2</sub>, <sup>13</sup>CH<sub>3</sub>/O, OH, H<sub>2</sub>O, <sup>13</sup>CO, <sup>13</sup>CHO, <sup>13</sup>CH<sub>2</sub>O, <sup>13</sup>CH<sub>3</sub>O/O<sub>2</sub>, <sup>13</sup>CH<sub>3</sub>OH and <sup>13</sup>CO<sub>2</sub> appear (Fig. 4e). So the C in CH<sub>3</sub>OH comes from CO<sub>2</sub> (reactant), rather than MWCNTs30. In Exp. III with <sup>12</sup>CO<sub>2</sub> and D<sub>2</sub>O as photoreduction reactants, *m/z* signals of H, D/H<sub>2</sub>, D<sub>2</sub>, CD, CD<sub>2</sub>/O, CD<sub>3</sub>/OD, OD, OH, D<sub>2</sub>O, CO, CDO, CD<sub>2</sub>O/O<sub>2</sub>, CD<sub>3</sub>O, CD<sub>3</sub>OH, CD<sub>3</sub>OD and CO<sub>2</sub> present, revealing that H<sub>2</sub>O is the origin for the H of CH<sub>3</sub> in CH<sub>3</sub>OH (Fig. 4f). There are two possible origins for the H of OH in CD<sub>3</sub>OH: COOH and OH groups on CdS/MWCNTs30. On CdS/MWCNTs0, COOH and OH also present, and OH content is 2.4-fold higher than COOH content (Table S1). But there is no CH<sub>3</sub>OH formed on CdS/MWCNTs0, indicating that the COOH and OH on CdS/MWCNTs0 cannot promote CH<sub>3</sub>OH formation. CdS/MWCNTs30 has a similar OH content to CdS/MWCNTs0, but much more COOH than CdS/MWCNTs0. The much higher COOH content could be responsible for the formation of CH<sub>3</sub>OH on CdS/MWCNTs30. Besides, in water solution, as compared with OH, deprotonation of COOH occurs more easily, and the proton of COOH can be more easily captured by CO<sub>2</sub> [36]. This implies that the COOH on CdS/MWCNTs30 could be the main source for the H of CD<sub>3</sub>OH in Exp. III, and could participate in forming CH<sub>3</sub>OH. Besides, during discharge-driven functionalization, COOH formation accompanies defect formation on MWCNTs30, with some defects close to COOH. Synergetic effect between COOH and defect may also contribute to CH<sub>3</sub>OH formation on CdS/MWCNTs30.

In Exps. IV and V, MWCNTs30 is prepared by conducting the discharge process with O<sub>2</sub> and D<sub>2</sub>O. This could create defect and COOH on MWCNTs30. In Exp. IV with <sup>12</sup>CO<sub>2</sub> and H<sub>2</sub>O as photoreduction reactants, *m/z* signals of H, H<sub>2</sub>/D, CH, CH<sub>2</sub>, CH<sub>3</sub>, O, OH, OD/H<sub>2</sub>O, CO, CHO, CH<sub>2</sub>O, CH<sub>3</sub>O, CH<sub>3</sub>OH/O<sub>2</sub>, CH<sub>3</sub>OD and CO<sub>2</sub> present (Fig. 4g). In Exp. V with <sup>12</sup>CO<sub>2</sub> and D<sub>2</sub>O as photoreduction reactants, *m/z* signals of D, D<sub>2</sub>, CD, CD<sub>2</sub>/O, CD<sub>3</sub>, OD, D<sub>2</sub>O, CO, CDO, CD<sub>2</sub>O/O<sub>2</sub>, CD<sub>3</sub>O, CD<sub>3</sub>OD, CD<sub>3</sub>OD and CO<sub>2</sub> present (Fig. 4h), without H-containing species. Exps. IV and V indicate that the H in COOH on MWCNTs30 could be involved in forming the OH of CH<sub>3</sub>OH, while H<sub>2</sub>O (reactant) provides H for forming both CH<sub>3</sub> and OH of CH<sub>3</sub>OH. In Exp. VI, MWCNTs is treated by discharge process with Ar only, and <sup>12</sup>CO<sub>2</sub> and H<sub>2</sub>O are used as photoreduction reactants. Due to the absence of H<sub>2</sub>O and O<sub>2</sub>, the Ar-discharge cannot create defect and COOH on MWCNTs, and the Ar-discharge-treated MWCNTs could be similar to MWCNTs0. In Exp. VI, *m/z* signals of H, H<sub>2</sub>, O, OH, H<sub>2</sub>O, CO, O<sub>2</sub> and CO<sub>2</sub> appear, but CH<sub>3</sub>OH-related species are absent (Fig. 4i). This confirms the crucial role of the defect and COOH on CdS/MWCNTs30 in forming CH<sub>3</sub>OH. In Exps. I-V, the weak CO signal could be caused by the CO<sub>2</sub> dissociation in mass spectrometer. The CO signal gets stronger in Exp. VI. Similar to MWCNTs0, Ar-discharge-treated MWCNTs could trigger CO production in photoreduction of CO<sub>2</sub> with H<sub>2</sub>O, thus enhancing CO signal in Exp. VI.

### 3.3. Discussions

Photoreduction of CO<sub>2</sub> with H<sub>2</sub>O proceeds mainly via the following steps: (i) light absorption by photocatalyst to form electron-hole pairs; (ii) electron-hole separation; (iii) reduction of CO<sub>2</sub> with the H formed in H<sub>2</sub>O splitting in the presence of photogenerated electrons [1–3,37–41]. To clarify the reason for the photoreduction product difference of CdS/MWCNTs30 from CdS/MWCNTs0, we compare the photocatalysts' ability in light absorption, electron-hole separation, CO<sub>2</sub> adsorption and H production. CdS/MWCNTs0 and CdS/MWCNTs30 have similar UV-visible spectra with an absorption edge (520 nm) which is due to CdS (Fig. S19) [36]. So the two photocatalysts have similar light absorption ability. As reflected by UPS and Mott-Schottky studies (Fig. S20), CdS/MWCNTs0 and CdS/MWCNTs30 have similar valence band, conduction band and band gap width (about 2.52 eV). Photocurrent is applied to study the photocatalysts' electron-hole separation



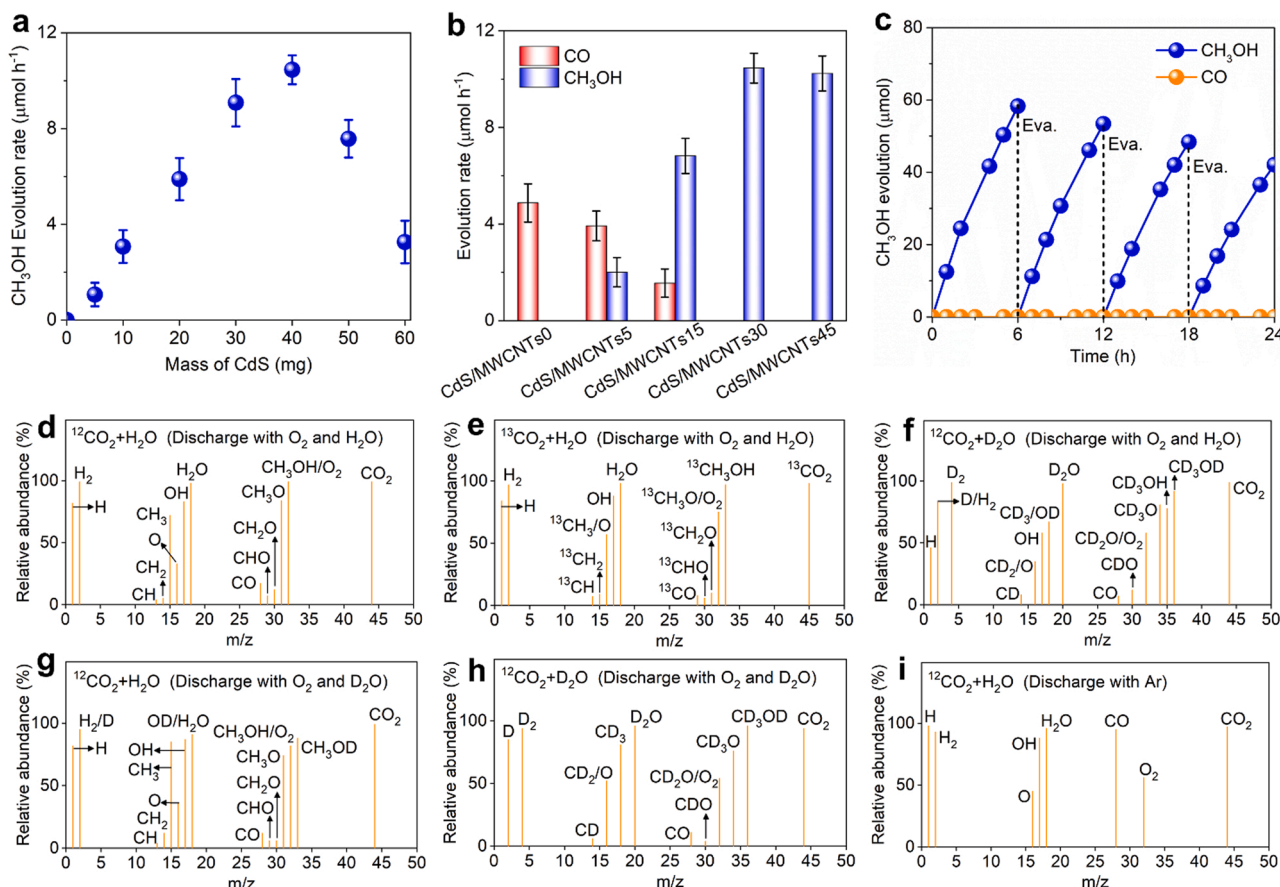


**Fig. 4.** (a) Change of CH<sub>3</sub>OH evolution rate as a function of CdS mass in CdS/MWCNTs30, with the mass of MWCNTs30 fixed at 10 mg. (b) CO and CH<sub>3</sub>OH evolution rates on different photocatalysts. (c) Stability of CdS/MWCNTs30 during the photoreduction of CO<sub>2</sub>. (d-i) Mass spectrometer signals for the photoreduction products on CdS/MWCNTs30 under different conditions.

efficiency (Fig. S21). A more efficient electron-hole separation leads to a higher photocurrent [35,36]. So the light absorption and band structure could not be the origin for the evident difference in photoreduction product between CdS/MWCNTs0 and CdS/MWCNTs30. CdS/MWCNTs0 and CdS/MWCNTs30 have higher photocurrents than pure CdS, indicating the enhanced electron-hole separation in the presence of MWCNTs0 and MWCNTs30. CdS/MWCNTs30 has a photocurrent (7.4 mA cm<sup>-2</sup>) slightly higher than that of CdS/MWCNTs0 (6.7 mA cm<sup>-2</sup>), revealing that CdS/MWCNTs30 is slightly more efficient in electron-hole separation than CdS/MWCNTs0. This could make some contributions to the evident difference in photoreduction product between CdS/MWCNTs0 and CdS/MWCNTs30.

There is no CO<sub>2</sub> adsorption on pure CdS (Fig. S22). CdS/MWCNTs30 has a CO<sub>2</sub> adsorption ability (1.89 mmol g<sup>-1</sup>) close to MWCNTs30 (1.92 mmol g<sup>-1</sup>), while CdS/MWCNTs0 has a CO<sub>2</sub> adsorption ability (0.82 mmol g<sup>-1</sup>) close to MWCNTs0 (0.83 mmol g<sup>-1</sup>) (Fig. S22). This reveals that MWCNTs0 and MWCNTs30 could provide active sites for CO<sub>2</sub> adsorption on CdS/MWCNTs0 and CdS/MWCNTs30, respectively. The CO<sub>2</sub> adsorption ability of CdS/MWCNTs30 is 2.3-fold higher than that of CdS/MWCNTs0. *In-situ* Raman spectra are recorded during the photoreduction of CO<sub>2</sub> on CdS/MWCNTs30 (Fig. 5a). The I<sub>D</sub>/I<sub>G</sub> ratio on Raman spectra, which reflects the carbon defect content on CdS/MWCNTs30, is 0.82 before triggering photoreduction (0 min) (Fig. 5a), and close to that on pure MWCNTs30 without CdS (0.83) (Fig. 1d). By elongating the photoreduction time, the I<sub>D</sub>/I<sub>G</sub> ratio decreases, and reaches to 0.20 after proceeding photoreduction for 30 min. Thus, the defect content on CdS/MWCNTs30 decreases during reaction, indicating that the defects on MWCNTs30 could be active sites for CO<sub>2</sub> adsorption and conversion on CdS/MWCNTs30.

DFT studies also demonstrate that the most active site for CO<sub>2</sub> adsorption and conversion on CdS/MWCNTs30 is the carbon defect close to COOH on MWCNTs30 (Fig. S23). The DFT model for simulating CdS/MWCNTs30 contains a COOH and two defects (Defect-1 and Defect-2) on MWCNTs30, with Defect-1 close to COOH and Defect-2 far away from COOH (Fig. 5b). There are 3 coordination unsaturated C and 9 coordination saturated C at each defect (Fig. 5b). DFT calculations show that Defect-1 has a higher electron density than other sites including Defect-2 (Fig. S24). The total Bader charge on the 12 C at Defect-1 (-0.136 e) is more negative than that at Defect-2 (-0.022 e) and other sites (Fig. 5c). This further reveals the higher electron density at Defect-1. After testing CO<sub>2</sub> adsorption at various sites on CdS/MWCNTs30 by DFT studies, we find that CO<sub>2</sub> prefers to adsorb at Defect-1, with the adsorption energy at Defect-1 (0.29 eV) larger than those at Defect-2 (0.21 eV) and other sites (Fig. 5b). This agrees well with the *in-situ* Raman studies. Electron transfer from adsorbent to CO<sub>2</sub> is the force to drive CO<sub>2</sub> adsorption, and the site rich in electrons on adsorbent favors for CO<sub>2</sub> adsorption [37–41]. So the preferred CO<sub>2</sub> adsorption at Defect-1 could be due to the higher electron density at Defect-1. In the CO<sub>2</sub> adsorption structure at Defect-1, the C atom of CO<sub>2</sub> bonds to a coordination unsaturated C atom (No. 1), with a bond of 1.46 Å (Fig. 5b). The adsorbed CO<sub>2</sub> (∠OCO: 150°, C–O bond: 1.3 Å) is distorted from the free CO<sub>2</sub> in gas phase (∠OCO: 180°, C–O bond: 1.2 Å), indicating the activation of the adsorbed CO<sub>2</sub>. The *in-situ* Raman and DFT studies show that the carbon defect on MWCNTs30 is the most active site for CO<sub>2</sub> adsorption on CdS/MWCNTs30. Therefore, the higher CO<sub>2</sub> adsorption ability of CdS/MWCNTs30 could be due to its higher carbon defect content. In addition, DFT studies show that the coordination unsaturated C at Defect-1 is also the most active site for H<sub>2</sub>O adsorption and

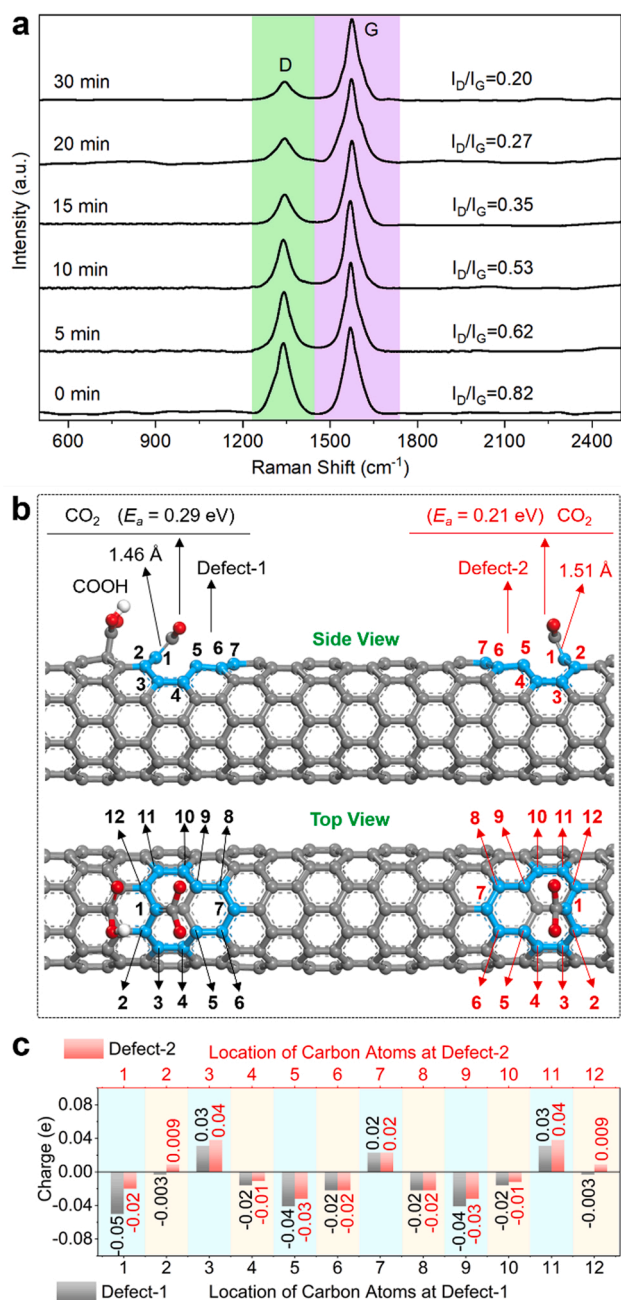


**Fig. 5.** (a) *In-situ* Raman spectra recorded during the photoreduction on CdS/MWCNTs30. (b) DFT-calculated CO<sub>2</sub> adsorption structures on CdS-decorated MWCNTs with one COOH and two defects. (c) Bader charges on the C at Defect-1 and Defect-2. The numbers of C in Fig. 5c correspond to the numbers in Fig. 5b.

dissociation on CdS/MWCNTs30 (Fig. S25).

On the *in-situ* FTIR spectra recorded during CO<sub>2</sub> adsorption on CdS/MWCNTs30, the peaks at 1690, 1525, 1460 and 1420 cm<sup>-1</sup> are due to the adsorbed CO<sub>2</sub> (CO<sub>2</sub>\*), while the peak at 1650 cm<sup>-1</sup> is caused by OCOH\* (Fig. 6a) [42,43]. The FTIR peaks of CO<sub>2</sub>\* and OCOH\* appear at 1 and 2 min, respectively, and become stronger at longer adsorption times. Thus, during the CO<sub>2</sub> adsorption on CdS/MWCNTs30, CO<sub>2</sub>\* could be formed firstly, and then converted into OCOH\*. The *in-situ* FTIR spectra of CdS/MWCNTs0 only show CO<sub>2</sub>\* peaks, no matter how long the adsorption is (Fig. 6b). In addition, the FTIR peaks on CdS/MWCNTs0 are much weaker than those on CdS/MWCNTs30. Therefore, CdS/MWCNTs0 has a lower CO<sub>2</sub> adsorption ability than CdS/MWCNTs30, and cannot hydrogenate CO<sub>2</sub> into OCOH\*. There are

two possible origins for the H in OCOH\* on CdS/MWCNTs30: COOH and OH groups on MWCNTs30. On CdS/MWCNTs0, COOH and OH present, and the OH content is 2.4 times higher than the COOH content (Table S1). However, there is no OCOH\* formed on CdS/MWCNTs0, indicating that the COOH and OH on CdS/MWCNTs0 cannot result in OCOH\*. CdS/MWCNTs30 has a similar OH content to CdS/MWCNTs0, but much more COOH than CdS/MWCNTs0. The evidently increased COOH could be responsible for the OCOH\* formation on CdS/MWCNTs30. Besides, as revealed by *in-situ* Raman spectra and DFT calculations, CO<sub>2</sub> is preferred to adsorb at the carbon defect close to COOH. This facilitates the transfer of H from COOH to CO<sub>2</sub>. Thus, the COOH could be the origin for the OCOH\* formation on CdS/MWCNTs30.

DFT calculations are next conducted to study how COOH and defect affect CO<sub>2</sub> reduction (Fig. 6c and 6d). Intermediates formed during the reactions are given (Fig. S26). On the photocatalyst with a COOH and two defects (Defect-1 and Defect-2), the CO<sub>2</sub>\* at Defect-1 prefers to abstract the H of COOH close to Defect-1 to form OCOH\*, with an energy barrier of 0.38 eV and a reaction energy of -0.12 eV (exothermic reaction) (Fig. 6c). This shows the crucial role of COOH in forming OCOH\*. On the photocatalyst without COOH and defect, the CO<sub>2</sub>\* abstracts an H from H<sub>2</sub>O splitting to form OCOH\* with a reaction energy of 0.11 eV (endothermic reaction) and an energy barrier of 0.51 eV (Fig. 6d). This is more difficult than that on the photocatalyst with COOH and defect. This agrees well with the *in-situ* FTIR spectra. There are three possible fates for OCOH\*, i.e. (i) hydrogenated into HOCOH\*, (ii) hydrogenated into OCHOH\* and (iii) dissociated into CO. On the photocatalyst with COOH and defects, hydrogenating OCOH\* into HOCOH\* by abstracting an H from H<sub>2</sub>O splitting at Defect-1 proceeds more easily than the formation of OCHOH\* and CO (Fig. 6c and S26). HOCOH\* can be flexibly split into COH\* and OH\* via an exothermic reaction with a reaction energy of -0.27 eV, and COH\* can be easily hydrogenated into CH<sub>3</sub>OH by abstracting H atoms from H<sub>2</sub>O splitting at Defect-1 (Fig. S27). Thus, on the photocatalyst with COOH and defects, CH<sub>3</sub>OH formation is more favorable than the formation of CO. The H in HOCOH\* is from both COOH on photocatalyst and H<sub>2</sub>O, indicating that the H in COH\* and OH of CH<sub>3</sub>OH are originated from either COOH on photocatalyst or H<sub>2</sub>O. This agrees well with the isotopic experiments. On the photocatalyst without COOH and defect, dissociation of OCOH\* into CO is more easily than the hydrogenation of OCOH\* into HOCOH\* and OCHOH\* (Fig. 6d and S26). Thus, formation of CO is more favored on the photocatalyst without COOH and defect.

The above results show that the COOH and defect on the photocatalyst are crucial for forming CH<sub>3</sub>OH in the photoreduction of CO<sub>2</sub> with H<sub>2</sub>O. The poor activity of CdS/MWCNTs0 in producing CH<sub>3</sub>OH could be due to its lower COOH and defect contents. However, too many COOH could occupy carbon defects active for CO<sub>2</sub> adsorption and conversion, thus lowering CO<sub>2</sub> conversion efficiency. We analyze the relationship of CH<sub>3</sub>OH evolution rate with defect/COOH contents on MWCNTs calculated from XPS spectra (Table S1). As shown in Fig. S28, with defect/COOH contents on MWCNTs becoming higher, the CH<sub>3</sub>OH evolution rate increases firstly, and then decreases slightly. The highest CH<sub>3</sub>OH evolution rate is achieved in the presence of MWCNTs30. Therefore, the COOH and defect contents on MWCNTs30 could be the most appropriate for forming CH<sub>3</sub>OH. According to CO<sub>2</sub> adsorption experiment, *in-situ* Raman and FTIR spectra as well as DFT calculations, on CdS/MWCNTs30, the carbon defects are active sites for enhancing CO<sub>2</sub> adsorption, and COOH close to carbon defects provide H to promote CO<sub>2</sub> reduction to CH<sub>3</sub>OH. These could be an origin for the overturning of the photoreduction product from CO on CdS/MWCNTs0 to CH<sub>3</sub>OH on CdS/MWCNTs30.

During photoreduction of CO<sub>2</sub> with H<sub>2</sub>O, H<sub>2</sub> evolution is the main competitive process for CO<sub>2</sub> reduction, as it consumes H and photo-generated electrons which are the key species for reducing CO<sub>2</sub> [37–41]. During photocatalytic H<sub>2</sub>O splitting in the absence of CO<sub>2</sub>, H<sub>2</sub> and O<sub>2</sub> evolution rates on CdS/MWCNTs30 are 38.6 and 6.1 μmol h<sup>-1</sup>,



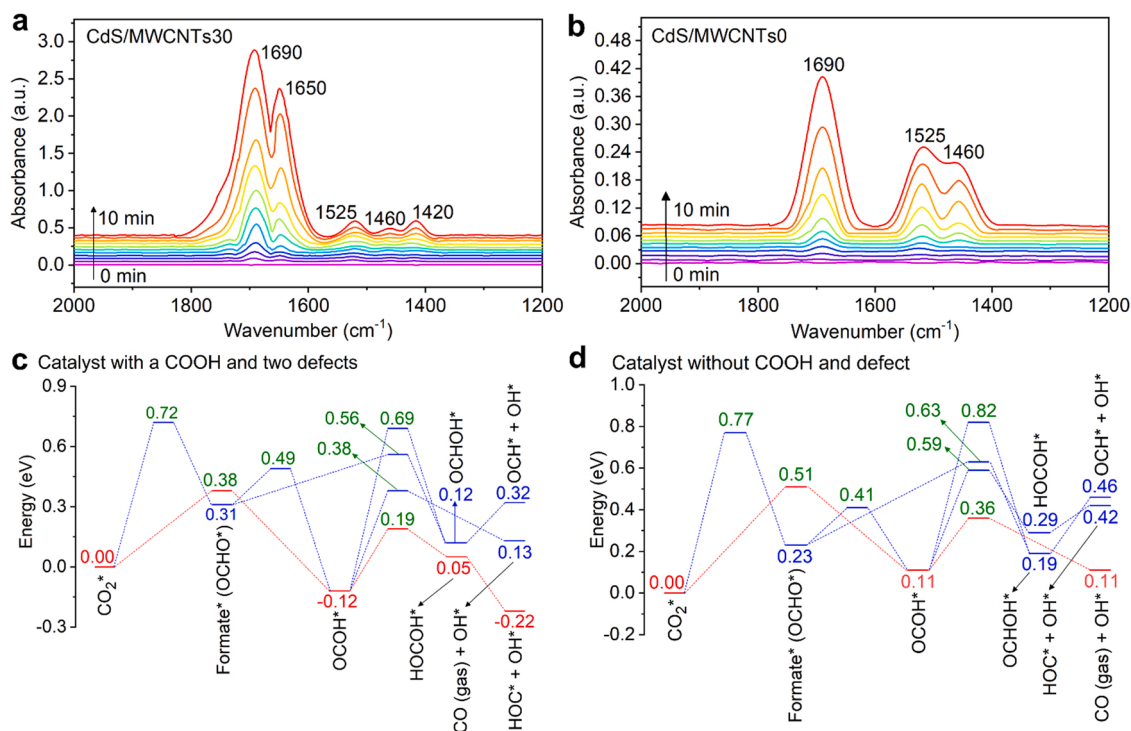


**Fig. 6.** (a) *In-situ* FTIR spectra for CO<sub>2</sub> adsorption on CdS/MWCNTs30. (b) *In-situ* FTIR spectra for CO<sub>2</sub> adsorption on CdS/MWCNTs0. (c) DFT-calculated energy profiles for CO<sub>2</sub> hydrogenation on photocatalyst with COOH and defects. (d) DFT-calculated energy profiles for CO<sub>2</sub> hydrogenation on photocatalyst without COOH and defect. The green numbers in (c, d) denote the relative energies (eV) of transition states for reactions, as compared with CO<sub>2</sub>\*. The blue numbers in (c, d) denote the relative energies (eV) of intermediates and products for reactions, as compared with CO<sub>2</sub>\*. The red lines in (c) and (d) denote the most favorable pathways for CO<sub>2</sub>\* conversion.

respectively, while those on CdS/MWCNTs0 are 24.7 and 4.9  $\mu\text{mol h}^{-1}$ , respectively (Fig. S29). So CdS/MWCNTs30 has a higher activity to splitting H<sub>2</sub>O. As reflected by DFT calculations (Fig. S25), carbon defect is the most favorable site for H<sub>2</sub>O splitting on the photocatalyst. The higher activity of CdS/MWCNTs30 in H<sub>2</sub>O splitting could be due to its higher defect content. In photoreduction of CO<sub>2</sub> with H<sub>2</sub>O, the evolution rates of H<sub>2</sub> and O<sub>2</sub> on CdS/MWCNTs30 are 18.5 and 4.7  $\mu\text{mol h}^{-1}$ , respectively, while those on CdS/MWCNTs0 are 15.1 and 3.2  $\mu\text{mol h}^{-1}$ , respectively (Fig. S29). Part of H from H<sub>2</sub>O splitting are consumed by CO<sub>2</sub> reduction, thus decreasing the H<sub>2</sub> evolution rate as compared with those in the reaction without CO<sub>2</sub>. The OH groups or/and O atoms from H<sub>2</sub>O splitting may be adsorbed on carbon defect of photocatalyst to form groups like C-O-C and C=O. This suppresses O<sub>2</sub> formation, thus leading O<sub>2</sub> evolution rates to be not match the stoichiometric ratio. The H combination to form H<sub>2</sub> and H transfer to the adsorbed CO<sub>2</sub> on different photocatalysts are studied by DFT calculations (Fig. S30). On photocatalyst without COOH and defect, H<sub>2</sub> formation is exothermic, with an energy barrier of 0.71 eV, while H transfer to the adsorbed CO<sub>2</sub> is endothermic, with an energy barrier of 0.95 eV. On photocatalyst with COOH and defects, H<sub>2</sub> formation is endothermic, with an energy barrier of 0.89 eV, while H transfer to the adsorbed CO<sub>2</sub> is exothermic, with an energy barrier of 0.58 eV. Thus, the photocatalyst with COOH and defects suppresses H combination but promotes more H to take part in CO<sub>2</sub> hydrogenation. The defect and COOH enhance CO<sub>2</sub> adsorption and activation, thus making the adsorbed CO<sub>2</sub> have a higher ability in abstracting H. The suppressed H combination could create an H-rich environment favoring for forming CH<sub>3</sub>OH. This could be another origin for the overturning of the photoreduction product from CO on CdS/MWCNTs0 to CH<sub>3</sub>OH on CdS/MWCNTs30.

During the photoreduction without sacrificial reagents, the photo-generated electrons are involved in CO<sub>2</sub> reduction, while the photo-generated holes could be consumed by the following processes: (i) reaction between holes and OH to form O<sub>2</sub> and (ii) capturing by carbon

defects rich in electrons or/and negatively charged O-containing functional groups (e.g. OH<sup>-</sup> and COO<sup>-</sup>). In addition, carbon defects on MWCNTs30 are active sites for CO<sub>2</sub> adsorption and conversion. With the photoreduction proceeding, desorption of the photoreduction product from carbon defects leads to the recovery of carbon defects, thus triggering further adsorption and conversion of CO<sub>2</sub>. This could be the origin for the stable performance of CdS/MWCNTs30 in the 24 h reaction (Fig. 4c).

#### 4. Conclusions

In summary, we functionalize pristine MWCNTs0 with carbon defects and COOH groups to form MWCNTs30 via a novel discharge process. In photoreduction of CO<sub>2</sub> with pure H<sub>2</sub>O in the absence of sacrificial reagent, with CdS as light absorber, MWCNTs30 triggers a selective CH<sub>3</sub>OH production, with a CH<sub>3</sub>OH selectivity of 100% and an IQE of 3.9%, but the C-based product in the presence of MWCNTs0 is CO. The carbon defects are active sites for CO<sub>2</sub> adsorption, and the COOH groups close to carbon defects provide H to promote CO<sub>2</sub> hydrogenation to CH<sub>3</sub>OH. The carbon defects and COOH groups enhance H<sub>2</sub>O splitting to form H and H transfer to CO<sub>2</sub>, thus boosting CO<sub>2</sub> hydrogenation to CH<sub>3</sub>OH. The multiple roles of carbon defects and COOH groups could be responsible for overturning the photoreduction product from CO on CdS/MWCNTs0 to CH<sub>3</sub>OH on CdS/MWCNTs30. These results open a new way to achieve selective photoreduction of CO<sub>2</sub> in the absence of sacrificial reagents and noble metals.

#### CRediT authorship contribution statement

**Peng Liu:** Conceptualization, Methodology, Investigation, Writing – original draft. **Lin Niu:** Investigation, Validation. **Yu-Long Men:** Investigation, Resources. **Chong Peng:** Software, Validation. **Zheng Liu:** Data analyses, Validation, Revising. **Xin-Yu Meng:** Investigation,

**Validation.** Yun-Xiang Pan: Conceptualization, Methodology, Supervision, Writing – review & editing, Project administration, Funding acquisition.

## Declaration of Competing Interest

The authors declare that they have no known competing financial interests or personal relationships that could have appeared to influence the work reported in this paper.

## Acknowledgement

This work is supported by National Natural Science Foundation of China (No. 21922807, 22078193, 22122807).

## Appendix A. Supporting information

Supplementary data associated with this article can be found in the online version at doi:10.1016/j.apcatb.2022.121985.

## References

- Y. Wang, R. Godin, J.R. Durrant, J. Tang, Efficient hole trapping in carbon dot/oxygen-modified carbon nitride heterojunction photocatalysts for enhanced methanol production from CO<sub>2</sub> under neutral conditions, *Angew. Chem. Int. Ed.* 60 (2021) 20811–20816.
- W. Zhang, A.R. Mohamed, W.-J. Ong, Z-scheme photocatalytic systems for carbon dioxide reduction: where are we now? *Angew. Chem. Int. Ed.* 59 (2020) 22894–22915.
- G. Chen, G.I.N. Waterhouse, R. Shi, J. Zhao, Z. Li, L.-Z. Wu, C.-H. Tung, T. Zhang, From solar energy to fuels: recent advances in light-driven C<sub>1</sub> chemistry, *Angew. Chem. Int. Ed.* 58 (2019) 17528–17551.
- A. Zhou, Y. Dou, C. Zhao, J. Zhou, X.-Q. Wu, J.-R. Li, A leaf-branch TiO<sub>2</sub>/carbon@MOF composite for selective CO<sub>2</sub> photoreduction, *Appl. Catal. B: Environ.* 264 (2020), 118519.
- H.-B. Huang, Z.-B. Fang, R. Wang, L. Li, M. Khanpour, T.-F. Liu, R. Cao, Engineering hierarchical architecture of metal-organic frameworks for highly efficient overall CO<sub>2</sub> photoreduction, *Small* 18 (2022), 2200407.
- S. Wang, M. Xu, T. Peng, C. Zhang, T. Li, I. Hussain, J. Wang, B. Tan, Porous hypercrosslinked polymer-TiO<sub>2</sub>-graphene composite photocatalysts for visible-light-driven CO<sub>2</sub> conversion, *Nat. Commun.* 10 (2019) 676.
- Q. Wang, J. Warnan, S. Rodríguez-Jiménez, J.J. Leung, S. Kalathil, V. Andrei, K. Domen, E. Reisner, Molecularly engineered photocatalyst sheet for scalable solar formate production from carbon dioxide and water, *Nat. Energy* 5 (2020) 703–710.
- B. Debnath, S. Singh, S.M. Hossain, S. Krishnamurthy, V. Polshettiwar, S. Ogale, Visible light-driven highly selective CO<sub>2</sub> reduction to CH<sub>4</sub> using potassium-doped g-C<sub>3</sub>N<sub>5</sub>, *Langmuir* 38 (2022) 3139–3148.
- B.K. Woan, G. Pyrgiotakis, W. Sigmund, Photocatalytic carbon-nanotube-TiO<sub>2</sub> composites, *Adv. Mater.* 21 (2009) 2233–2239.
- Q. Liu, C. Zeng, Z. Xie, L. Ai, Y. Liu, Q. Zhou, J. Jiang, H. Sun, S. Wang, Cobalt@nitrogen-doped bamboo-structured carbon nanotube to boost photocatalytic hydrogen evolution on carbon nitride, *Appl. Catal. B: Environ.* 254 (2019) 443–451.
- Y. Wang, Q. Cai, M. Yao, S. Kang, Z. Ge, X. Li, Easy synthesis of ordered mesoporous carbon-carbon nanotube nanocomposite as a promising support for CO<sub>2</sub> photoreduction, *ACS Sustain. Chem. Eng.* 6 (2018) 2529–2534.
- M. Shu, Z. Zhang, Z. Dong, J. Xu, CsPbBr<sub>3</sub> perovskite quantum dots anchored on multiwalled carbon nanotube for efficient CO<sub>2</sub> photoreduction, *Carbon* 182 (2021) 454–462.
- Y.-L. Men, P. Liu, X. Peng, Y.-X. Pan, Efficient photocatalysis triggered by thin carbon layers coating on photocatalysts: Recent progress and future perspectives, *Sci. China Chem.* 63 (2020) 1416–1427.
- V. Bogdanovskaya, I. Vernigor, M. Radina, V. Sobolev, V. Andreev, N. Nikolskaya, Modified carbon nanotubes: surface properties and activity in oxygen reduction reaction, *Catalysts* 11 (2021) 1354.
- R. Wang, H. Wu, R. Chen, Y. Chi, Strong electrochemiluminescence emission from oxidized multiwalled carbon nanotubes, *Small* 15 (2019), 1901550.
- Z. Wang, Y. Zhang, E.C. Neyts, X. Cao, X. Zhang, B.W.-L. Jang, C.-J. Liu, Catalyst preparation with plasmas: How does it work? *ACS Catal.* 8 (2018) 2093–2110.
- N. Rui, X. Zhang, F. Zhang, Z. Liu, X. Cao, Z. Xie, R. Zou, S.D. Senanayake, Y. Yang, J.A. Rodriguez, C.-J. Liu, Highly active Ni/CeO<sub>2</sub> catalyst for CO<sub>2</sub> methanation: Preparation and characterization, *Appl. Catal. B: Environ.* 282 (2021), 119581.
- Y.-L. Men, P. Liu, Y. Liu, X.-Y. Meng, Y.-X. Pan, Noble-metal-free WO<sub>3</sub>-decorated carbon nanotubes with strong W-C bonds for boosting an electrocatalytic glucose oxidation reaction, *Ind. Eng. Chem. Res.* 61 (2022) 4300–4309.
- U.R. Kortshagen, R.M. Sankaran, R.N. Pereira, S.L. Girshick, J.J. Wu, E.S. Aydil, Nonthermal plasma synthesis of nanocrystals: fundamental principles, materials, and applications, *Chem. Rev.* 116 (2016) 11061–11127.
- E. Picheau, A. Impellizzeri, D. Rybkovskiy, M. Bayle, J.-Y. Mevellec, F. Hof, H. Saadaoui, L. Noé, A.C.T. Dias, J.-L. Duvail, M. Monthieux, B. Humbert, P. Puech, C.P. Ewels, A. Pénicaud, Intense Raman D band without disorder in flattened carbon nanotubes, *ACS Nano* 15 (2021) 596–603.
- X. Zhang, P. Yang, S.P. Jiang, Ni diffusion in vertical growth of MoS<sub>2</sub> nanosheets on carbon nanotubes towards highly efficient hydrogen evolution, *Carbon* 175 (2021) 176–186.
- B. Zhang, M. Clausi, B. Heck, S. Laurenzi, M.G. Santonicola, J. Kleperis, A. Antuzevičs, G. Reiter, A.N. Aleshin, A.S. Lobach, Changes in surface free energy and surface conductivity of carbon nanotube/polyimide nanocomposite films induced by UV irradiation, *ACS Appl. Mater. Interfaces* 13 (2021) 24218–24227.
- S. Ali, S.A.U. Rehman, I.A. Shah, M.U. Farid, A.K. An, H. Huang, Efficient removal of zinc from water and wastewater effluents by hydroxylated and carboxylated carbon nanotube membranes: behaviors and mechanisms of dynamic filtration, *J. Hazard. Mater.* 365 (2019) 64–73.
- M.U. Farid, H.-Y. Luan, Y. Wang, H. Huang, A.K. An, R.J. Khan, Increased adsorption of aqueous zinc species by Ar/O<sub>2</sub> plasma-treated carbon nanotubes immobilized in hollow-fiber ultrafiltration membrane, *Chem. Eng. J.* 325 (2017) 239–248.
- Y. Xing, L. Li, C.C. Chusuei, R.V. Hull, Sonochemical oxidation of multiwalled carbon nanotubes, *Langmuir* 21 (2005) 4185–4190.
- L.G. Bulusheva, A.V. Okotrub, E. Flahaut, I.P. Asanov, P.N. Gevko, V.O. Koroteev, Y.V. Fedoseeva, A. Yaya, C.P. Ewels, Bromination of double-walled carbon nanotubes, *Chem. Mater.* 24 (2012) 2708–2715.
- C. Duong-Viet, Y. Liu, H. Ba, L. Truong-Phuoc, W. Baaziz, L. Nguyen-Dinh, J.-M. Nhut, C. Pham-Huu, Carbon nanotubes containing oxygenated decorating defects as metal-free catalyst for selective oxidation of H<sub>2</sub>S, *Appl. Catal. B: Environ.* 191 (2016) 29–41.
- J.L. Figueiredo, M.F.R. Pereira, M.M.A. Freitas, J.J.M. Órfão, Modification of the surface chemistry of activated carbons, *Carbon* 37 (1999) 1379–1389.
- H. Liu, P. Sun, M. Feng, H. Liu, S. Yang, L. Wang, Z. Wang, Nitrogen and sulfur co-doped CNT-COOH as an efficient metal-free catalyst for the degradation of UV filter BP-4 based on sulfate radicals, *Appl. Catal. B: Environ.* 187 (2016) 1–10.
- S.-M. Xue, Z.-L. Xu, Y.-J. Tang, C.-H. Ji, Polypiperazine-amide nanofiltration membrane modified by different functionalized multiwalled carbon nanotubes (MWCNTs), *ACS Appl. Mater. Interfaces* 8 (2016) 19135–19144.
- S. Deng, X. Liu, J. Liao, H. Lin, F. Liu, PEI modified multiwalled carbon nanotube as a novel additive in PAN nanofiber membrane for enhanced removal of heavy metal ions, *Chem. Eng. J.* 375 (2019), 122086.
- Z. Khazaei, A.R. Mahjoub, A.H.C. Khavar, One-pot synthesis of CuBi bimetallic alloy nanosheets-supported functionalized multiwalled carbon nanotubes as efficient photocatalyst for oxidation of fluoroquinolones, *Appl. Catal. B: Environ.* 297 (2021), 120480.
- Y. Zhang, Y. Wu, L. Wan, H. Ding, H. Li, X. Wang, W. Zhang, Hollow core-shell Co<sub>9</sub>S<sub>8</sub>@ZnIn<sub>2</sub>S<sub>4</sub>/CdS nanoreactor for efficient photothermal effect and CO<sub>2</sub> photoreduction, *Appl. Catal. B: Environ.* 311 (2022), 121255.
- Z. Fang, J. Zhou, Y. Sun, J. Hu, L. Liang, R. Xu, H. Duan, Homoepitaxial growth on semiconductor nanocrystals for efficient and stable visible-light photocatalytic hydrogen evolution, *Nanoscale* 9 (2017) 17794.
- Z. Fang, Y. Wang, J. Song, Y. Sun, J. Zhou, R. Xu, H. Duan, Immobilizing CdS quantum dots and dendritic Pt nanocrystals on thiolated graphene nanosheets toward highly efficient photocatalytic H<sub>2</sub> evolution, *Nanoscale* 5 (2013) 9830–9838.
- L. Zhu, Y. Liu, X. Peng, Y. Li, Y.-L. Men, P. Liu, Y.-X. Pan, Noble-metal-free CdS nanoparticle-coated graphene oxide nanosheets favoring electron transfer for efficient photoreduction of CO<sub>2</sub>, *ACS Appl. Mater. Interfaces* 12 (2020) 12892–12900.
- C. Li, Y. Xu, W. Tu, G. Chen, R. Xu, Metal-free photocatalysts for various applications in energy conversion and environmental purification, *Green. Chem.* 19 (2017) 882–899.
- X.-Y. Meng, C. Peng, J. Jia, P. Liu, Y.-L. Men, Y.-X. Pan, Recent progress and understanding on In<sub>2</sub>O<sub>3</sub>-based composite catalysts for boosting CO<sub>2</sub> hydrogenation, *J. CO<sub>2</sub> Util.* 55 (2022), 101844.
- Y.-X. Pan, Y. You, S. Xin, Y. Li, G. Fu, Z. Cui, Y.-L. Men, F.-F. Cao, S.-H. Yu, J. B. Goodenough, Photocatalytic CO<sub>2</sub> reduction by carbon-coated indium-oxide nanobelts, *J. Am. Chem. Soc.* 139 (2017) 4123–4129.
- F. Arcudi, L. Đorđević, B. Nagasing, S.I. Stupp, E.A. Weiss, Quantum dot-sensitized photoreduction of CO<sub>2</sub> in water with turnover number > 80,000, *J. Am. Chem. Soc.* 143 (2021) 18131–18138.
- S. Barman, A. Singh, F.A. Rahimi, T.K. Maji, Metal-free catalysis: a redox-active donor-acceptor conjugated microporous polymer for selective visible-light-driven CO<sub>2</sub> reduction to CH<sub>4</sub>, *J. Am. Chem. Soc.* 143 (2021) 16284–16292.
- Q. Li, Z. Sun, H. Wang, Z. Wu, Insight into the enhanced CO<sub>2</sub> photocatalytic reduction performance over hollow-structured Bi-decorated g-C<sub>3</sub>N<sub>4</sub> nanohybrid under visible-light irradiation, *J. CO<sub>2</sub> Util.* 28 (2018) 126–136.
- D. Xiang, D. Magana, R.B. Dyer, CO<sub>2</sub> reduction catalyzed by mercaptopteridine on glassy carbon, *J. Am. Chem. Soc.* 136 (2014) 14007–14010.